Computer-aided pulmonary disease diagnosis using lung ultrasound video

Saeful Bahri [a,c,1,*], Suprijanto [b,2], Endang Juliastuti [b,3]

[a] Doctoral Program of Engineering Physics, Faculty of Industrial Technology, Institut Teknologi Bandung, Jalan Ganesa No.10, Bandung, 40132, Indonesia
[b] Instrumentation and Control Research Group, Faculty of Industrial Technology, Institut Teknologi Bandung, Jalan Ganesa No.10, Bandung, 40132, Indonesia
[c] Department of Electrical Engineering, Faculty of Engineering, Universitas Muhammadiyah Jakarta, Jalan Cempaka Putih Tengah 27, Jakarta, 10510, Indonesia
[1] saeful.bahri@umj.ac.id; [2] supri89@itb.ac.id; [3] yuliast@itb.ac.id
* corresponding author

ARTICLE INFO

Article history
Received November 01, 2023
Revised June 02, 2024
Accepted June 15, 2024
Available online December 30, 2024

Keywords
Computer-aided diagnosis
Lung ultrasound
Machine learning
Pneumonia
COVID-19

ABSTRACT

The development of a machine learning-based computer-aided diagnosis (CAD) system implemented for processing lung ultrasound images will greatly assist doctors in making decisions in diagnosing lung diseases. The learning method of the classifier model used in the computer-aided diagnosis system will affect the system's accuracy in diagnosing lung disease. Determining variables in the classifier and image pre-processing stages requires special attention to obtain a highly accurate classifier model. This study presents the development of a machine learning-based CAD as an add-on tool to classify lung disease based on a lung ultrasound (LUS) video. The main steps in this study are capturing the LUS videos and converting them into images, image pre-processing for speckle noise removal, image contrast and brightness enhancement, feature extraction, and the classification stage. In this study, three learning algorithm models, namely Support Vector Machine (SVM), K-Nearest Neighbor (KNN), and Naïve Bayes (NB), were used to classify images into three categories, namely healthy conditions, pneumonia, and COVID-19. The performance of the three classifier models is compared to each other to obtain the best classifier model. The experimental results demonstrate the superiority of the suggested strategy utilizing the SVM classifier. Based on experimental data using 2,149 lung images for three classes and 20 texture feature sets, the SVM has an accuracy of 98.1%, the KNN is 94.7%, and the Gaussian NB is 79.6%. The model with the highest accuracy will be used to develop the computer-aided diagnosis (CAD) system.

1. Introduction

Pneumonia is one of the world's most frequent pathological ailments. It is a lung infection caused by viruses, bacteria, or fungi that attack one or both lungs, resulting in inflammation and swelling of the air sacs in the lungs (alveoli) [1]. Pneumonia is one of the main problems in the health sector worldwide, including in Indonesia, especially pneumonia in children. Pneumonia is the first cause of death from an infectious disease in toddlers and has claimed the lives of more than 800,000 children under five every year, or about 2,200 every day worldwide [2]. One of the problems with diagnosing pneumonia is the symptoms vary widely and are similar to those seen in influenza. Consequently, it is challenging to

diagnose [3]. Consequently, effective diagnosis and monitoring of lung disorders are essential and need to be developed to assist doctors in diagnosing lung diseases.

Medical imaging applications in hospitals and laboratories have demonstrated benefits in seeing patient's internal organs for illness diagnosis and therapy. Ultrasound (US), as the safest medical imaging tool, assists in disease therapy. Medical researchers have shown that ultrasound has several advantages over CXR and CT. Compared to CT and CXR, the US is considered safer, especially for pediatric patients. It is free of ionizing radiation, and the examination costs are cheaper. It is easy to use and possible for rapid and repeated examination. It is generally available in almost all modern healthcare centers [4]. In addition, an ultrasound examination can also be implemented directly on the patient without the need to move the patient to the radiology room [5]. Ultrasound is proven to have higher sensitivity and accuracy when compared to chest X-rays [6].

Since the 1990s, practically all specialist offices have used point-of-care ultrasonography [7]. Point-of-care ultrasound (POCUS) involves using and interpreting ultrasound (US) at the patient's bedside rather than transferring the patient to a scanning room [8]. Its application in the emergency department is expanding due to its practical, safe, and beneficial benefits [9]. During the COVID-19 pandemic and the development of ultrasound devices that are increasingly moving toward compact and portable forms, the use of POCUS as a diagnostic modality has increased because it is considered more practical and widely used, particularly in the handling of patients in emergency departments who require rapid action [10]–[14].

Lung ultrasound (LUS) has several problems, as with other US techniques. It is operator-dependent [6], [8], and the interpretation of LUS images is generally based on qualitative and subjective observations made manually by radiologists [15]. It affects US image interpretation results' accuracy, consistency, efficiency, and reliability. In addition, lung ultrasound is a medical imaging process that looks for artifacts that characterize or signify lung abnormalities. It is difficult to recognize because the artifact obtained may be due to lung abnormalities or image-taking errors.

Artifacts are images that include information unrelated to a specific anatomical component but can give valuable input if correctly identified. Lung US could identify a normal lung, pleural effusion, pneumothorax, pulmonary atelectasis/consolidation, pulmonary edema, diaphragm paresis or paralysis, and pulmonary embolism are some of the disorders. Numerous respiratory diseases are recognized based on artifacts shown on ultrasound images, namely pleural lines, A-lines, B-lines, consolidation, and pleural effusion.

With an average sensitivity of over 90%, ultrasound has the potential to detect lung abnormalities by detecting B-lines, pleural line abnormalities, and consolidation [6], [16]. Although ultrasonography had better sensitivity than chest X-ray, other researchers discovered it had worse specificity [6]. This fact puts researchers on the spot to increase the specificity of ultrasonography. Supported by the rapid development of medical imaging technology, computer-aided diagnosis (CAD) assists us in solving diagnosing problems. As a well-trained expert, it has a broad application prospect when needed to close the experience gap.

Comparative studies have been conducted to compare the effectiveness of two approaches that can be used in a computer-aided diagnostics system using classical and deep learning approaches [17]. The study showed that although the deep learning approach performed very well in identifying and selecting features, the deep learning approach has a drawback related to the large amount of data required to train

the model. Meanwhile, the availability of extensive data is not guaranteed to be fulfilled. Even if we could gather a large amount of data, a new problem arises: choosing the data to make an efficient system with no under-fitting or over-fitting phenomenon. In the case of limited datasets, classical methods are the best choice [17].

This study aimed to develop a computer-aided diagnosis (CAD) system called CAD-LUS, designed as an add-on tool to classify lung disease based on LUS videos. The system diagnoses and categorizes lung diseases into healthy lungs, pneumonia, and viral pneumonia (COVID-19). The lung video was acquired using various ultrasonography (USG) machines with either a linear or convex probe. The suggested method is derived from a machine-learning model using multi-frame images as input. Three classifier algorithms, Support Vector Machine (SVM), K-Nearest Neighbor (KNN), and Naïve Bayes (NB), are used and compared to classify LUS video into three classes: healthy, pneumonia, and COVID-19. This approach was trained and verified using a publicly available LUS dataset [18]. The proposed CAD system is one of the efforts to improve specificity, which is one of the shortcomings in the use of LUS, as mentioned in [7]–[9]. Of course, it still has high accuracy and sensitivity as well.

The remainder of this paper is a summary: section 2 describes the proposed method. Section 3 explains the results of various categorization approaches, discussions, and comparisons. The research conclusions are presented in Section 4 of this study report.

2. Method

A computer-aided diagnosis (CAD) assists us in solving the diagnosing problem existing in the current method, which highly depends on personal experience. As a well-trained expert, it has a broad application prospect when needed to close the experience gap. This study presents an image classification challenge for computer-aided diagnosis of lung disorders using ultrasound imaging data. The task involves categorizing ultrasound pictures into three categories in lung disease cases. The approach has three main components: pre-processing, feature extraction, and classification, as seen in Fig. 1. The multi-class classifier model was used to classify lung conditions into three categories: normal or healthy lung, pneumonia, and viral pneumonia (COVID-19).

The hardware and software for the computer-aided diagnosis (CAD) were performed using the Python-based program Spyder v4.1.5 on an MSI laptop equipped with an Intel(R) Core (TM) i5-10200H CPU @ 2.40GHz, 16 GB RAM, and a Laptop GPU NVIDIA GeForce RTX 3060.

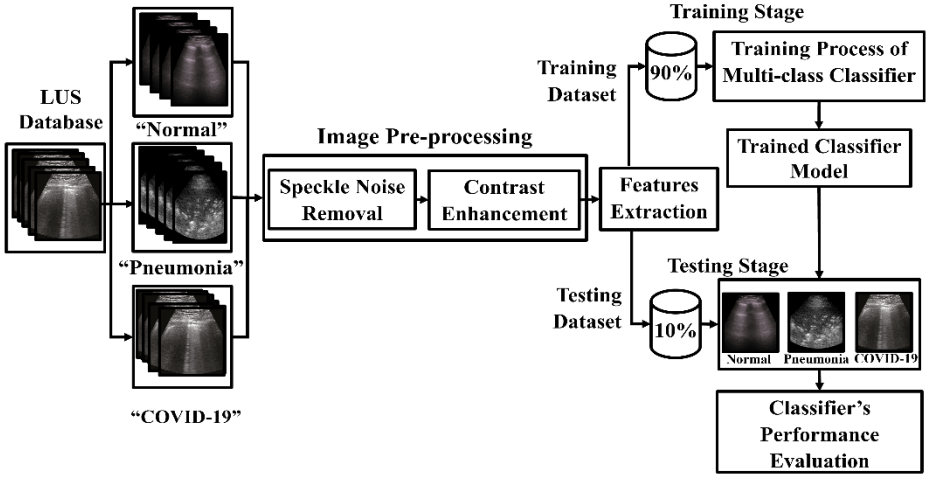

Fig. 1. The computer-aided diagnosis of pulmonary disorders based on lung ultrasound images

2.1. Dataset Description

To train and validate the classifier model in a computer-aided diagnosis system, a publicly available and freely accessible ultrasound video recordings database compiled by [18] has been used. The database contains some lung ultrasounds in video format and images obtained using linear and convex transducers collected from several sources and hospitals (operated by various operators and using different ultrasound machines). The ultrasound video data comprised 56 videos for healthy lungs, 36 for pneumonia, and 30 for COVID-19 (122 total video data).

Symptoms, such as physical characteristics of lung diseases, must be linked to image attributes when using a CAD system. Professionals do this association manually or automatically using the CAD system itself. In both circumstances, the learning process is the foundation for diagnostic aid. The success of this stage is determined by the pictures used for training, the discriminating features chosen, the correctness of the image annotation, and the objectivity of the hand annotation process.

In general, ultrasound images of normal lungs are characterized by repetitive horizontal lines called A-lines that are regularly spaced. Reverberation or multiple reflections from the pleural layer produce these A-lines, whose distance is equal to the distance between the skin layer and the pleural layer. The horizontal A-lines created by multiple reflections of the pleural line have the same interval distance as the distance between the skin and the pleura. The presence of the continuous and regular pleural line and A-line artifacts indicated a normal lung [19].

Irregularities in the A-line pattern distinguish lung problems. Furthermore, more severe pulmonary disorders are characterized by the appearance of vertical lines known as B-lines. These are vertical linear artifacts caused by pleural lines reflecting additional elements with large acoustic impedance gradients around the pleural layer, such as fluid or air, and the disappearance of the A-line. Multiple B-lines are a sonographic marker of lung interstitial syndrome, and their number rises as air content decreases and lung density increases. ARDS (Acute Respiratory Distress Syndrome) is distinguished by an inhomogeneous bilateral pattern of several coalescent B-lines and white lungs, which may be accompanied by scattered spared patches. B-lines in COVID-19 pneumonia are depicted in their potential patterns [20].

Volpicelli et al. [21] state lung peripheral consolidations have subpleural echo-poor or tissue-like echotexture. They may include air or fluid bronchograms, vertical artifacts at the far-field boundary, or hepatization. Consolidations with B-lines are typical ultrasonography patterns seen in patients with ARDS. Early viral pneumonia is characterized by a few, generally bilateral, pulmonary lung sections with single or bundled pneumogenic-type vertical artifacts or tiny patches of white lung. Advanced COVID-19 pneumonia exhibits consolidations, particularly in the post-erobasal areas, and patchy artifactual alterations. This pattern is comparable to that found in ARDS [19]. Fig. 2 shows a sample of healthy lungs, pneumonia, and COVID-19 obtained using linear and convex probes.

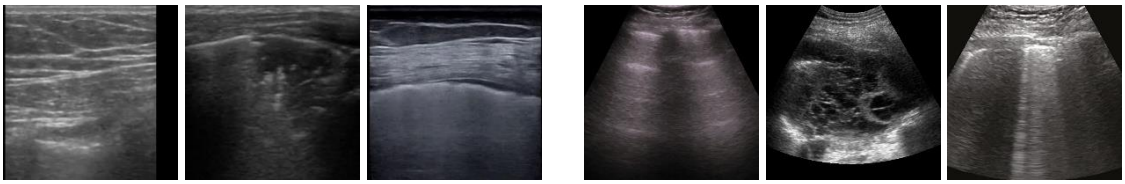

(a) (b)

Fig. 2. Sample LUS images for normal, pneumonia, and COVID-19 with probe type (a) linear, (b) convex

2.2. Image pre-processing

The frame capture process converted the raw lung ultrasound data in video format from multiple sources [18] into images taken from video frames in the pre-processing stage. The total number of images obtained during this conversion process could estimated by multiplying the video framerate (frame per second) value by the time recordings. Because the ultrasound video recordings in the database have non-uniform fps and recording time, the training and validating model was performed using only a portion by specifying the appropriate fresh rate value.

Because the lung ultrasound video recordings have varying frame rates and recording lengths, the LUS video data extracted every one-third of its fps maximum. The size of the ultrasound video recording will determine the amount of images utilized. The longer the recording length of each video, the more images are used. However, to reduce the quantity of data handled, this study restricts the maximum number of frames from each video to 30 frames for each video data. Besides frame rates and recording lengths, the pixel sizes in the original image source data also vary. All images are of varying shapes and sizes, and image size homogeneity is normalized to 128x128 pixels before the feature extraction procedure is performed.

Most ultrasound image pre-processing and analysis methods seek to minimize speckle content and enhance features to improve structure visibility and clinical interpretation. One of the methods for removing speckle noise is a spatial-based approach that is applied directly to the original image. The image filter in spatial domain methods directly manipulates the value of the pixel intensity of the picture plane based on the algorithm used. The techniques applied to image filters in this approach are the Frost filter [22], median filter [23], and Speckle Reduction Anisotropic Diffusion (SRAD), which exploits local statistical features in the denoising process [24]. This approach computes the weighted average of the square window for each image's noisy pixel.

The image obtained from the LUS video conversion process has a varied and inhomogeneous contrast, affecting the quality of the image. CLAHE, or Contrast Limited Adaptive Histogram Equalization, is one of the valuable methods to improve image quality. CLAHE's remarkable performance in medical imaging [25]. CLAHE might improve blurring caused by speckle filtering in ultrasound images [25]. The CLAHE method divides the images into several non-overlapping, almost equal-sized portions [26]. The first step in this procedure is computing the histogram of each area. Then, a clip limit for clipping histograms is calculated depending on a chosen contrast expansion limit. Furthermore, to optimize the contrast range dynamic of images resulting from the CLAHE process [26] using Power law transformations and formulated in (1) where c is a constant, and s and r represent the pixels' gray levels in the output and input images, respectively.

$$S = C\, r^{\gamma} \tag{1}$$

2.3. Features extraction

The image classification process links characteristics to known features in image processing using rules developed in connection to a set of numerical criteria of an image that describe the item or phenomena. These criteria describe visual qualities, and their extraction comprises mathematical transformations applied to the pixels of a digital image. The challenge of such a classification problem mainly lies in selecting distinguishable features. Thus, most researchers have focused on the feature design of various types, such as texture features.

The texture represents a local spatial variation in pixel intensities and orientation. It is a critical characteristic utilized for object recognition in an image's area of interest (ROI) to obtain distinctive characteristics that characterize the inner intensity distribution of different classes in images using texture analysis. Texture feature descriptors are computed using a variety of structural, spectral, and statistical model-based methodologies, including the gray-level histogram, run-length matrix, gray-level co-occurrence matrix (GLCM), and contourlet transform coefficient.

GLCM is a popular statistical texture analysis technique that examines regional textures utilizing second-order texture characteristics. Several researchers discovered that the Grey-Level Co-occurrence Matrix (GLCM) method for extracting ultrasound image features produced good results because the classifier model performed well [27]–[30]. The process utilizes 14 types of textural features in the GLCM feature extraction technique [31]. These textural properties might characterize the item under investigation. GLCM was computed using four directions of closeness, mostly 0^0, 45^0, 90^0, and 135^0, with texture elements such as energy, contrast, entropy, correlation, and homogeneity, as has been done in [32].

GLCM can calculate texture features by taking the position distribution of pixels with the same gray level. Equation (2) calculates the GLCM matrix for a gray-scale image I size N × N [17]. The shift operator $(\Delta x, \Delta y)$ represents the pixel position that may be applied to any image pixel.

$$P(i,j) = \sum_{x=0}^{N-1} \sum_{y=0}^{N-1} \begin{cases} 1, & if\ I(x,y) = i\ and\ I\ (x+\Delta x, y+\Delta y) = j \\ 0, & otherwise \end{cases} \quad (2)$$

The foremost necessary parameters to determine GLCM texture features are computed using the co-occurrence matrices generated by equation (2). In our work, the GLCM features, i.e., correlation, energy, entropy, contrast, and homogeneity, are selected for lung disease classification. These features are mathematically formulated by the following equations.

$$Correlation = \sum_{i,j=0}^{N-1} P(i,j) \frac{(i-\mu)(j-\mu)}{\sigma^2} \quad (3)$$

μ and σ represent the mean and standard deviation, respectively.

$$Energy = \sum_{i,j=0}^{N-1} (P(i,j)^2 \quad (4)$$

$$Entropy = \sum_{i,j=0}^{N-1} -P(i,j) log P(i,j) \quad (5)$$

$$Contrast = \sum_{i,j=0}^{N-1} (i-j)^2 P(i,j) \quad (6)$$

$$Homogeneity = \sum_{i,j=0}^{N-1} P(i,j) \frac{P(i,j)}{1+(i-j)^2} \quad (7)$$

2.4. Image classification

The final stage in the computer-aided diagnosis process is the classification of lung images based on imaging features. Image classification refers to relating attributes to known features in image processing. The image classifier is the algorithm that influences the classification process. These classifiers, driven by machine learning algorithms, will build predictive models to map the image features into predefined groups and classes. So far, models are presented as classification rules, decision trees, or mathematical functions.

This work used the classifiers Support vector machines, k-nearest neighbor, and Gaussian naive Bayes to classify lung diseases based on lung ultrasound videos. The feature extraction procedure yields a twenty-feature vector for each input image. As a result, in the feature extraction process, Nx20-feature vectors are produced from N-images. These feature vectors were divided into two portions, with 90% of the total feature vectors utilized to train the classifier and the remaining 10% used to asses the classifier performance. Each feature vector was labeled as "0" for healthy lungs, "1" for pneumonia, and "2" for COVID-19 throughout the training phase.

The classifier observes data patterns during the training phase. During training, the classifier extracts 20 attribute vectors (corresponding to 20 features) from the Nx20-feature vectors. These 20 attribute vectors were used as a reference to set the classification rules for classifying the training images for 2,149 lung ultrasound images. So, the whole data feature set used as classifier input is 2,149x20.

2.4.1. Support vector machine

Support vector machine (SVM) is a linear classifier or a two-class classification model. A binary or SVM classifier is confined initially to only two classifications. However, additional research has shown that SVM can be utilized as a multi-class classifier to classify data into several classes [15], [33]. SVM's multi-class classification scheme could be implemented by binary classification for each category. The binary classification model will distinguish that class from all others and build as many binary models as the number of types supplied. It is easier to design a binary classifier to discriminate between only two classes in an issue than to examine more than two classes in a problem since the decision boundary is more straightforward. As the impact, the binarization strategies for dealing with multi-class situations have evolved.

Researchers presented many solutions to the multiclassification problem using the SVM classifier, including one-versus-all (OVA) and one-versus-one (OVO), one of which has been implemented [34]. The OVA method develops a classifier for each class, where the class will be discriminated from all other classes. The base classifier that delivers a positive answer is indicated as the output class. To address the multiclassification problem utilizing OVA, k binary SVM classifiers are built, where k is the number of classes. Each classifier separates one class from the others, reducing the problem to a two-class issue. By using the k equation of the decision function $w_1^T \emptyset(x_1) + b_1; \ldots; w_k^T \emptyset(x_i) + b_k$, the final label output is assigned to the class with the highest output value.

$$Class\ of\ x = arg \max_{i=1,2,\ldots,k} (w_i^T \emptyset(x) + b_i \tag{8}$$

One-versus-one (OVO) splits the problem into as many binary problems as feasible between all conceivable class pair combinations so that one classifier is learned to differentiate between each pair. Then, the outputs of these base classifiers are merged to predict the output class. OVO constructs k(k - 1)/2 binary SVMs, each of which is utilized to differentiate just two of the k-classes and necessitates the assessment of (k - 1) SVM classifiers. The constraints for $(x_t y_t)$ for training data from the classes are:

$$\min_{w^{ij}, b^{ij}, \xi^{ij}} \frac{1}{2}(w^{ij})^T w^{ij} + C \sum_t \xi_t^{ij} (w^{ij})^T$$

$$(w^{ij})^T \phi(x_t) + b^{ij} \geq 1 - \xi_t^{ij}, if\ y_t = i$$

$$(w^{ij})^T \phi(x_t) + b^{ij} \geq -1 + \xi_t^{ij}, if\ y_t = i$$

$$\xi_t^{ij} \geq 0 \tag{9}$$

Each binary classifier will process an input feature (pattern) during validation. The binary classifier's output is given as $\mathbf{r}_{ij}$ Here, $\mathbf{r}_{ij} \in \{0,1\}$ is the binary classifier's confidence value that distinguishes between class-i and class-j of all classification classes formed.

As shown in equation (10), the total output of binary classification results between classes is represented in the score matrix [34], produced by each binary classifier's results.

$$SM = \begin{pmatrix} - & \boldsymbol{r}_{12} & \cdots & \boldsymbol{r}_{1k} \\ \boldsymbol{r}_{12} & - & \cdots & \boldsymbol{r}_{2k} \\ \vdots & \vdots & \ddots & \vdots \\ \boldsymbol{r}_{k1} & \boldsymbol{r}_{k2} & \cdots & - \end{pmatrix} \tag{10}$$

The aggregation model employed in (11) determines the system's final output depending on the data on the above score matrix [34].

$$Class\ of\ x = \arg \max_{i=1,2,..,k} \sum_{1 \leq j \neq i \leq m} S_{ij}$$

$$S_{ij} = 1\ if\ \boldsymbol{r}_{ij} > \boldsymbol{r}_{ji,\ and}\ S_{ij} = 0\ if\ \boldsymbol{r}_{ij} < \boldsymbol{r}_{ji} \tag{11}$$

2.4.2. K-nearest neighbor

The K-nearest neighbor (KNN) model is a non-parametric supervised machine learning approach commonly used for pattern classification and regression issues. KNN is a fundamental and straightforward classifier that can be implemented. It only takes a little memory to store data and performs well in multi-model classes [35].

K-nearest neighbor (KNN) is a classification approach for novel objects based on their k-nearest neighbors. The KNN classifier is highly sensitive when classifying medical images [36]. KNN is a supervised learning technique that categorizes the outcomes of new query instances based on most categories in KNN. The algorithm assigns the latest data to a class or category in the data set (training data) based on its closeness or similarities in a defined range (K) of neighbors. The class with the most appearances will be the class of classification results. The KNN algorithm's classification stages are as follows.

Step 1) Determine the number of neighbors (K) that will be considered as a class determination consideration; Step 2) Determine the distance between the new data and each data point in the dataset; Step 3) Sort the values of the distance computation results from least to most excellent, $di \leq di + 1$, where $i = 1, 2, 3, \ldots, k$; Step 4) Take K data points sorted in Step 3; Step 5) Identifies the new data class based on the most significant number of label frequencies.

If the KNN algorithm employs the Euclidean distance technique to calculate the distance between two data points, the Euclidean distance is defined by (12).

$$d(x_1, x_2) = \sqrt{\sum_{i=1}^{n} (x_{2i} - x_{1i})^2} \tag{12}$$

Where $d(x_1, x_2)$ is Euclidean distance, x_{1i} and x_{2i} are the i-th features of each existing labeled data and the i-th features of new data, respectively, and n is the number of features.

2.4.3. Naïve Bayes

The Naïve Bayes model is a supervised learning algorithm based on Bayes' Theorem that makes the "Naive" assumption of conditional independence between each pair of feature values of a particular class variable. It is straightforward to comprehend and create, the image data set can be trained, and computations take less time [35].

Bayes' Theorem asserts that the probability of a feature vector $(x_1 \dots x_n)$ being in class y is [37]:

$$P(y|x_1, x_2, \dots, x_n) = \frac{P(y)P(x_1, x_2, \dots, x_n|y)}{P(x_1, x_2, \dots, x_n)} \quad (13)$$

$$P(x_i|y, x_1, \dots, x_{i-1}, x_{i+1}, x_n) = \prod_{i=1}^{n} P(x_1|y) \quad (14)$$

Because $(x_1, x_2, \dots, x_n)$ are independent of one another, for all i values, the equation in (13) may be simplified as follows:

$$P(y|x_1, x_2, \dots, x_n) = \frac{P(y)\prod_{i=1}^{n} P(x_i|y)}{P(x_1, x_2, \dots, x_n)} \quad (15)$$

Adding proportionality by deleting the $P(x_1 \dots x_n)$ which is constant:

$$P(y|x_1, x_2, \dots, x_n) \propto P(y)\prod_{i=1}^{n} P(x_i|y) \quad (16)$$

Therefore, the classifier's output against the provided feature vector is given by:

$$\hat{y} = arg \max_{y} P(y)\prod_{i=1}^{n} P(x_i|y) \quad (17)$$

$P(y)$ and $P(x_i|y)$ may be estimated using Maximum A Posteriori (MAP). The assumptions used for the various forms of Naïve Bayes classifiers will vary depending on the distribution function of $P(x_i|y$ utilized. The distribution function $P(x_i|y$ in Gaussian Naïve Bayes (GaussianNB) is a Gauss distribution function formulated in (18), with μ as the mean value and σ as the standard deviation.

$$P(x_i|y) = \frac{1}{\sqrt{2\pi\sigma_y^2}} exp\left(-\frac{(x_i-\mu_y)^2}{2\sigma_y^2}\right) \quad (18)$$

3. Results and Discussion

This work employed three multi-class classifier models to classify lung ultrasound images. The first model is a Support Vector Machine (SVM) classifier with Gaussian kernel, C=10, and gamma=100. The second model is the K-Nearest Neighbor (KNN) classifier with $k = 1$, distance metric= "Euclidean," and weights metric=" equal." The last model is the Naïve Bayes (NB) classifier using a Gaussian distribution function.

The proposed computer-aided diagnosis method classifies 2,149 images converted from 122 lung ultrasound videos containing 56 healthy lung data, 36 pneumonia data, and 30 videos of COVID-19 data. The overall number of frame images acquired was 2,149, with 524 COVID-19 data, 463 pneumonia image data, and 1,162 healthy lung image data:

3.1. Performance evaluation metrics

The confusion matrix was used to assess classifier performance throughout the training phase. The model's performance, such as accuracy, precision, recall, and F1-score, are calculated using the classification parameters of the classifier's prediction results in each class or category (TPi, TNi, FPi, and FNi) on the confusion matrix. Mathematical formulas for computing performance metrics of the model's performance are given by:

- Accuracy: the ratio of correct predictions (positive and negative). The accuracy of the i-th class is given by;

$$Accuracy = \left(\frac{T_{Pi}+T_{Ni}}{T_{Pi}+T_{Ni}+F_{Pi}+F_{Ni}}\right) \quad (19)$$

The average accuracy is estimated using the formula;

$$Avr_{ACC} = \frac{\sum_{i=1}^{C}\frac{T_{Pi}+T_{Ni}}{T_{Pi}+T_{Ni}+F_{Pi}+F_{Ni}}}{C} \quad (20)$$

- Precision: describes the degree of accuracy between the required data and the model's expected output. Precision is the ratio of positive correct predictions to total positive desired results. The precision equation is as follows;

$$Precision = \frac{T_{Pi}}{(T_{Pi}+F_{Pi})} \quad (21)$$

- Recall, known as sensitivity, describes the model's ability to retrieve information. Sensitivity is the ratio of true positive predictions to total true positive data. The following equation determines the recall value;

$$Sensitivity = \frac{T_{Pi}}{(T_{Pi}+F_{Ni})} \quad (22)$$

- Specificity: calculates the percentage of negative cases that are appropriately categorized as such. A high specificity indicates that the algorithm effectively recognizes negative examples, i.e., having a low false positive rate. Instead, a low specificity suggests that the algorithm is poor at detecting negative cases and has a high false positive rate. The specificity is determined using;

$$Specificity = \frac{T_{Ni}}{(T_{Ni}+F_{Pi})} \quad (23)$$

- F1-score: the harmonic mean of accuracy and sensitivity. F1-Score has a most significant value of 1.0 and a worst value of 0. For example, a classifier with a high F1-score value implies the classifier model has high accuracy and sensitivity. F1-score formulated by;

$$F1 - score = \frac{2^{*}(Precision*Sensitivity)}{(Precision+Sensitivity)} \quad (24)$$

3.2. Classification results

The GLCM matrix in the feature extraction stage is generated with d = 1 and θ= 0, 45, 90, and 135 degrees to investigate classifier performance. The learning and testing process was estimated using 2,149 images, with each image including 20 qualities to identify each class. Each feature vector is labeled with

"0" for the healthy lung class, "1" for the pneumonia class, and "2" for the COVID-19 class throughout the training phase. Confusion matrices of these classifiers are constructed by utilizing 90% of the dataset to train the model and testing on 10% of the dataset. The results in the confusion matrices for the SVM, KNN, and NB classifiers are provided in Fig. 3.

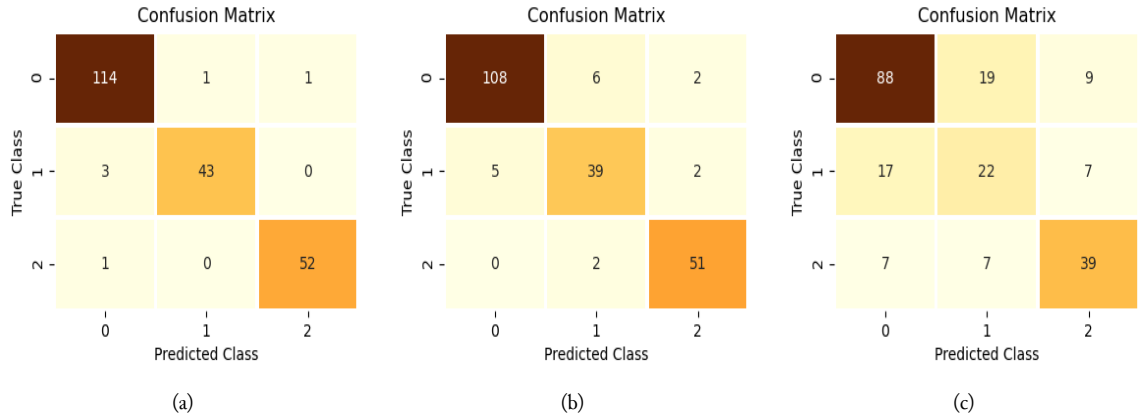

(a) (b) (c)

Fig. 3. The confusion matrices: (a) SVM classifier (b) KNN classifier (c) NB classifier

It is preferable to have a confusion matrix that has only diagonal entries for accurate categorization of test images. Entries outside the confusion matrix's diagonal represent the misclassification of test images. When a substantial percentage of test images fall outside the diagonal elements of the confusion matrix, the classifier's performance degrades. The results in Fig. 3(b) and Fig. 3(c) demonstrate that the number of images outside the diagonal elements rises when compared to Fig. 3(a). The number of images placed on the diagonal elements in Fig. 3(c) is significantly higher than in Fig. 3(b) and Fig. 3(c). As a consequence, the SVM classifier outperforms the other two classifiers.

Four parameters, designated true positive (TP), true negative (TN), false positive (FP), and false negative (FN), are computed from the classifier confusion matrix to create a measurable metric for categorizing individual classes. Table 1, Table 2, and Table 3 show the classification parameters of predicted images of an i-th category.

Table 1. The aggregate of true/false for the SVM classifier

Class	TP_i	TN_i	FP_i	FN_i
0	114	95	4	2
1	43	168	1	3
2	52	161	1	1
Σ	TP=209	TN=424	FP=6	FN=6

Table 2. The aggregate of true/false for the KNN classifier

Class	TP_i	TN_i	FP_i	FN_i
0	108	94	5	8
1	39	161	8	7
2	51	158	4	2
Σ	TP=198	TN=413	FP=17	FN=17

Table 3. The aggregate of true/false for the NB classifier

Class	TP_i	TN_i	FP_i	FN_i
0	88	75	24	28
1	22	143	26	24
2	39	146	16	14
Σ	TP=149	TN=364	FP=66	FN=66

The aggregate true/false values (TP, TN, FP, FN) of Table 1, Table 2, and Table 3 corresponding to the provided data set were used to estimate each classifier's performance parameters (precision, sensitivity, specificity, f1-score, and accuracy). Table 4 provides the performance parameters of the SVM classifier.

Table 4. The performance of the SVM classifier

Class	Accuracy	Precision	Sensitivity	Specificity	F1-score
0	0.972	0.966	0.983	0.960	0.974
1	0.981	0.977	0.935	0.994	0.956
2	0.991	0.981	0.981	0.994	0.981

The performance parameters of the KNN classifier are shown in Table 5, and Table 6 shows the performance parameters of the NB classifier. The classifiers' performance in terms of accuracy, precision, sensitivity, specificity, and f1-score were calculated using equation (13)-(18) based on the values of (TPi, TNi, FPi, and FNi) given in Table 1, Table 2, and Table 3.

Table 5. The performance of the KNN classifier

Class	Accuracy	Precision	Sensitivity	Specificity	F1-score
0	0.940	0.956	0.931	0.949	0.943
1	0.930	0.830	0.848	0.952	0.839
2	0.972	0.927	0.962	0.975	0.944

Table 6. The performance of the NB classifier

Class	Accuracy	Precision	Sensitivity	Specificity	F1-score
0	0.758	0.786	0.759	0.758	0.772
1	0.767	0.458	0.478	0.846	0.468
2	0.860	0.709	0.736	0.901	0.722

Based on performance data from Table 4, Table 5, and Table 6, the SVM method achieved the best accuracy, 97.2% for normal lung images, 98.1% for pneumonia, and 99.1% for COVID-19, compared to other classification methods. The KNN approach had an accuracy of 94.0% for normal lung images, 93.0% for pneumonia, and 97.2% for COVID-19. In contrast, the NB method had an accuracy of 75.8% for normal lung images, 76.7% for pneumonia, and 86.0% for COVID-19. As a result, the SVM classifier model has high accuracy in determining whether the supplied input LUS images are normal, pneumonia, or COVID-19.

According to the performance data, the SVM approach attained the best achievable precision, 96.6% for normal lung images, 97.7% for pneumonia, and 98.1% for COVID-19, compared to other classification algorithms. The KNN approach had a precision level of 95.6% for normal lung images,

83.0% for pneumonia, and 92.7% for COVID-19. In contrast, the NB method had a precision level of 78.6% for normal lung images, 45.8% for pneumonia, and 70.9% for COVID-19. As a result, the SVM correctly detects whether the supplied input LUS images are normal, pneumonia, or COVID-19.

According to the performance data, the SVM approach attained the best achievable sensitivity, 98.3% for normal lung images, 93.5% for pneumonia, and 98.1% for COVID-19, compared to other classification algorithms. The KNN approach had a sensitivity level of 93.1% for normal lung images, 84.8% for pneumonia, and 96.2% for COVID-19. In contrast, the NB method had a sensitivity level of 75.9% for normal lung images, 47.8% for pneumonia, and 73.6% for COVID-19. As a result, the SVM has a higher ability to retrieve information on whether the supplied input LUS images are normal, pneumonia, or COVID-19.

According to the performance data, the SVM method attained the best achievable specificity, 96.0% for normal lung images, 99.4% for pneumonia, and 99.4% for COVID-19, compared to other classification methods. The KNN approach had a specificity level of 94.9% for normal lung images, 95.3% for pneumonia, and 97.5% for COVID-19. In contrast, the NB method had a specificity level of 75.8% for normal lung images, 84.6% for pneumonia, and 90.1% for COVID-19. As a result, the SVM algorithm effectively recognizes negative examples of whether the supplied input LUS images are normal, pneumonia, or COVID-19.

According to the experimental data, the SVM method attained the best achievable f-1 score, 97.4% for normal lung images, 95.6% for pneumonia, and 98.1% for COVID-19, compared to other classification methods. The KNN approach had a f-1 score of 94.3% for normal lung images, 83.9% for pneumonia, and 94.4% for COVID-19. In contrast, the NB method had a f-1 score of 77.2% for normal lung images, 46.8% for pneumonia, and 72.2% for COVID-19. As a result, the SVM classifier model has high accuracy and sensitivity, regardless of whether the supplied input LUS images are normal, pneumonia, or COVID-19. Table 7 gives the average performance metrics value for SVM, KNN, and NB classifier data.

Table 7. The comparison of the classifier's performance

Classifier algorithm	Accuracy	Precision	Sensitivity	Specificity	F1-score
SVM	0.981	0.975	0.966	0.983	0.970
KNN	0.947	0.904	0.914	0.959	0.909
NB	0.796	0.651	0.658	0.835	0.654

The developed SVM model exhibited superior performance compared to other models, with 98.1% accuracy, 97.5% precision, 96.6% sensitivity, 98.3% specificity, and 97.0% F1-score. These values are comparable with other methods to classify the LUS images, as given in Table 8.

Table 8. The comparison of the techniques utilized to classify the LUS images

Authors	Accuracy	Sensitivity	Specificity	Precision	F1-score
Ghulam et al. [38]	0.925	0.932	-	0.918	-
Barros et al. [39]	0.930	0.970	1.000	1.000	0.950
Sadik et al. [40]	0.910	0.910	0.900	-	0.900
Awasthi et al. [41]	0.832	0.920	0.710	1.000	0.870
Proposed Method	0.981	0.966	0.983	0.975	0.970

Employing the POCUS lung ultrasound dataset [18], a study in [38] suggested a deep learning-based approach to categorize lung ultrasound images using 121 videos, 45 of which were COVID-19, 23 of which were bacterial pneumonia, and 53 were healthy. There were also 40 images: 18 for COVID-19, 7 for bacterial pneumonia, and 15 for healthy. They choose 30 frames per second for each video for maximum frame rate. Some videos have different recording times, with an average of 18±6 frames for each clip. The authors suggested a CNN model with multi-layer feature fusion [38], and the proposed approach has 92.5% accuracy.

Other researchers classify lung ultrasound (LUS) videos recorded with convex transducers [39]. They used the largest POCUS lung ultrasound dataset [42]. The authors suggested a hybrid methodology for diagnosing COVID-19 using a hybrid model named CNN-LSTM. This model extracts spatial characteristics using a convolutional neural network (CNN), while temporal dependency is learned using long- and short-term memory (LSTM). The suggested model has an average accuracy of 93% and a sensitivity of 97% for COVID-19.

An automated technique was presented to categorize LUS images into COVID-19, pneumonia, and regular/healthy categories using an efficient LUS image-enhancing scheme [40]. To minimize the noise in LUS images and to improve the performance of deep learning-based classification networks, they employ a spectral mask enhancement (SpecMEn) scheme and contrast-limited adaptive histogram equalization (CLAHE) in the pre-processing stage. They were using the POCUS lung ultrasound dataset [18] with 123 videos (41 for COVID-19, 27 for pneumonia, and 55 for healthy) and Deep CNN architectures (DenseNet-201, ResNet-152V2, Xception, VGG19, and NasNetMobile), the proposed scheme achieved 91% accuracy, 90% sensitivity, 90% specificity, and 90% F1-score.

While performing well, deep learning-based approaches have more computational complexity than machine learning methods. Large datasets are crucial for developing deep learning algorithms. They offer the essential training data to reflect the vast range of pathology-related presentations and data to thoroughly assess such systems' accuracy, robustness, and usefulness. When deployed, deep learning models are computationally heavy, and specific computer gear is necessary for real-time processing. It is needed because a more extensive annotated dataset is required to train the networks and pathologists for image interpretation [17].

Because of the computational complexity problem, a lightweight deep learning model for COVID-19 identification using lung US images has been developed [41]. The model classifies lung US images into COVID-19, pneumonia, and healthy cases. This assignment used a modified MobileNet model with focal loss, known as Mini-COVIDNet. Using 1103 lung US images (182 healthy, 277 pneumonia, and 678 COVID-19), the proposed network classifies all images in 24 minutes with an excellent accuracy of 83.2%.

Deep learning research generally centers on detecting the image produced by capturing an optical lens with distinguishing properties from ultrasound images. If identifying attribute features and segmentation is inadequate, the deep learning classifier will produce biased results throughout the feature extraction and pre-processing phases.

We develop a machine learning-based computer-aided diagnosis (CAD) to classify COVID-19, pneumonia, and healthy cases using LUS images. The contrast-limited adaptive histogram equalization (CLAHE) and gamma transform were employed in the pre-processing stage to minimize the noise in LUS images. This process is carried out to optimize the image pattern before the feature extraction

process to distinguish each category. Our proposed model achieves 98.1% accuracy, 97.5% precision, 96.6% sensitivity, 98.3% specificity, and 97.0% f1-score. These values were achieved by employing 20 features extracted using the GLCM method. Based on the investigation's findings, it is possible to infer that the proposed machine learning-based lung disease classification system is still reliable and efficient for classifying lung disorders (e.g., COVID-19, pneumonia, and healthy cases).

We developed and evaluated the model using a public dataset with heterogeneous characteristics (different hospitals, devices, and operators) so the results of this proposed model can be generalized to implement in different populations or settings.

4. Conclusion

The proposed computer-aided diagnosis (CAD) system could classify lung disorders into the healthy lung, pneumonia, and viral pneumonia (COVID-19). This suggested method is based on machine learning and consists of three main phases: image pre-processing, image feature extraction, and classification. The developed model analyzed lung ultrasound video obtained with linear and convex probes. The superiority of the suggested strategy utilizing the SVM classifier was proved by experimental results on 2149 lung ultrasound images. The proposed technique with 20 GLCM feature inputs and an SVM classifier yielded the most excellent classification average accuracy of 98.1%, 97.5% for precision, 96.6% for sensitivity, 98.3% for specificity, and 97.0% for f1-score. Finally, the proposed SVM classification model excellently classified lung disorders as healthy lung, pneumonia, and COVID-19. This fact gives a promising tool for further developing and perhaps improving the detection of lung disorders, especially in rural areas where access to reliable diagnosis is limited.

Although the developed SVM model performs best, this research has several limitations. First, this study utilized no method to determine the acquired images of the video files. All collected images were used entirely following the captures made for each video category. Second, the classifier model for constructing a CAD system was validated and tested using publicly available and freely accessible ultrasound video recording data. Geographically, the patient data utilized in the ultrasound recordings differ from the circumstances of the Indonesian population, particularly in the dimensions of both men's and women's body postures. For future work, the system must be tested using ultrasound recording data from patients in Indonesia for the model to be verified before it is used for direct identification and diagnosis, and the doctors can use this CAD system to assist them in lung disease diagnosis.

Acknowledgment

The authors would like to thank to Institut Teknologi Bandung for supporting this research. Additionally, the first author thank to the Department of Electrical Engineering, Faculty of Engineering, Universitas Muhammadiyah Jakarta, for supporting scholarships for the doctoral program in Engineering Physics at Institut Teknologi Bandung.

Declarations

Author contribution. All authors contributed equally to the paper's main contribution. The final article was read and approved by all authors

Funding statement. None of the authors have received funding or grants from any institution or funding body for the research

Conflict of interest. The authors declare no conflict of interest.

Additional information. No additional information is available for this paper.

References

[1] S. L. Contreras-Ojeda, C. Sierra-Pardo, J. A. Dominguez-Jimenez, J. Lopez-Bueno, and S. H. Contreras-Ortiz, "Texture Analysis of Ultrasound Images for Pneumonia Detection in Pediatric Patients," *2019 22nd Symp. Image, Signal Process. Artif. Vision, STSIVA 2019 - Conf. Proc.*, pp. 2019–2022, 2019, doi: 10.1109/STSIVA.2019.8730238.

[2] UNICEF, "Every Child's Right To Survive: An Agenda To End Pneumonia Deaths," 2020. [Online]. Available at: https://data.unicef.org/resources/every-childs-right-to-survive-an-agenda-to-end-pneumonia-deaths/.

[3] American Lung Association, "Pneumonia Symptoms and Diagnosis," 2020. [Online]. Available at: https://www.lung.org/lung-health-diseases/lung-disease-lookup/pneumonia/symptoms-and-diagnosis.

[4] J. Zhang *et al.*, "Detection and Classification of Pneumonia from Lung Ultrasound Images," pp. 294–298, 2020, doi: 10.1109/ccisp51026.2020.9273469.

[5] L. M. Xi, H. M. Yang, M. M. Bin, C. B. Weelic, and L. M. Ji-Bin, "Critical Care Ultrasonography and Its Application for COVID-19," *Adv. Ultrasound Diagnosis Ther.*, vol. 4, no. 2, p. 43, 2020, doi: 10.37015/audt.2020.200035.

[6] Y. I. Haggag, K. Mashhour, K. Ahmed, N. Samir, and W. Radwan, "Effectiveness of lung ultrasound in comparison with chest X-ray in diagnosis of lung consolidation," *Open Access Maced. J. Med. Sci.*, vol. 7, no. 15, pp. 2457–2461, 2019, doi: 10.3889/oamjms.2019.669.

[7] N. J. Soni, R. Arntfield, and P. D. Kory, "Evolution of Point-of-Care Ultrasound," in *Point-of-Care Ultrasound*, 2nd ed., Eds. Elsevier, Inc., 2020, pp. 1–394. [Online]. Available at: https://books.google.co.id/books?hl=en&lr=&id=1IYZBAAAQBAJ&oi=fnd&pg=PA3&dq=Evolution+of+Point-of-Care+Ultrasound+2nd.

[8] S. Kulkarni, B. Down, and S. Jha, "Point-of-care lung ultrasound in intensive care during the COVID-19 pandemic," *Clin. Radiol.*, vol. 75, no. 9, pp. 710.e1-710.e4, 2020, doi: 10.1016/j.crad.2020.05.001.

[9] F. Mojoli, B. Bouhemad, S. Mongodi, and D. Lichtenstein, "Lung ultrasound for critically ill patients," *Am. J. Respir. Crit. Care Med.*, vol. 199, no. 6, pp. 701–714, 2019, doi: 10.1164/rccm.201802-0236CI.

[10] D. Buonsenso, A. Piano, F. Raffaelli, N. Bonadia, K. de Gaetano Donati, and F. Franceschi, "Point-of-Care Lung Ultrasound findings in novel coronavirus disease-19 pnemoniae: A case report and potential applications during COVID-19 outbreak," *Eur. Rev. Med. Pharmacol. Sci.*, vol. 24, no. 5, pp. 2776–2780, 2020, doi: 10.26355/eurrev_202003_20549.

[11] M. Alkhafaji, T. Ward, and J. Truong, "A case of lung ultrasound findings in a 73-year-old male with COVID-19," *Vis. J. Emerg. Med.*, vol. 21, no. May, p. 100796, 2020, doi: 10.1016/j.visj.2020.100796.

[12] W. M. Peh, S. K. T. Chan, Y. L. Lee, P. S. Gare, and V. K. Ho, "Lung ultrasound in a singapore covid-19 intensive care unit patient and a review of its potential clinical utility in pandemic," *J. Ultrason.*, vol. 20, no. 81, pp. e154–e158, 2020, doi: 10.15557/JoU.2020.0025.

[13] A. Jahanshir, S. M. Moghari, A. Ahmadi, P. Z. Moghadam, and M. Bahreini, "Value of point-of-care ultrasonography compared with computed tomography scan in detecting potential life-threatening conditions in blunt chest trauma patients," *Ultrasound J.*, vol. 12, no. 1, pp. 6–15, 2020, doi: 10.1186/s13089-020-00183-6.

[14] N. Veronese, L. G. Sbrogiò, R. Valle, L. Marin, E. Boscolo Fiore, and A. Tiozzo, "Prognostic Value of Lung Ultrasonography in Older Nursing Home Residents Affected by COVID-19," *J. Am. Med. Dir. Assoc.*, vol. 21, no. 10, pp. 1384–1386, 2020, doi: 10.1016/j.jamda.2020.07.034.

[15] L. Carrer *et al.*, "Automatic Pleural Line Extraction and COVID-19 Scoring from Lung Ultrasound Data," *IEEE Trans. Ultrason. Ferroelectr. Freq. Control*, vol. 67, no. 11, pp. 2207–2217, 2020, doi: 10.1109/TUFFC.2020.3005512.

[16] Z. I. Bitar, O. S. Maadarani, A. A. M. El-Shably, and M. J. Al-Ajmi, "Diagnostic accuracy of chest ultrasound in patients with pneumonia in the intensive care unit: A single-hospital study," *Heal. Sci. Reports*, vol. 2, no. 1, pp. 1–6, 2019, doi: 10.1002/hsr2.102.

[17] R. Guetari, H. Ayari, and H. Sakly, "Computer-aided diagnosis systems: a comparative study of classical machine learning versus deep learning-based approaches," *Knowl. Inf. Syst.*, vol. 65, no. 10, pp. 3881–3921, 2023, doi: 10.1007/s10115-023-01894-7.

[18] J. Born *et al.*, "POCOVID-Net: Automatic Detection of COVID-19 From a New Lung Ultrasound Imaging Dataset (POCUS)," no. April, pp. 1-14, 2020. [Online]. Available at: https://europepmc.org/article/ppr/ppr268507.

[19] G. Soldati *et al.*, "Proposal for International Standardization of the Use of Lung Ultrasound for Patients With COVID-19," *J. Ultrasound Med.*, vol. 39, no. 7, pp. 1413–1419, 2020, doi: 10.1002/jum.15285.

[20] G. Volpicelli and L. Gargani, "Sonographic signs and patterns of COVID-19 pneumonia," *Ultrasound J.*, vol. 12, no. 1, pp. 20–22, 2020, doi: 10.1186/s13089-020-00171-w.

[21] G. Volpicelli *et al.*, "International evidence-based recommendations for point-of-care lung ultrasound," *Intensive Care Med.*, vol. 38, no. 4, pp. 577–591, 2012, doi: 10.1007/s00134-012-2513-4.

[22] R. K. Painam and M. Suchetha, "Despeckling of SAR Images Using BEMD-Based Adaptive Frost Filter," *J. Indian Soc. Remote Sens.*, vol. 51, no. 9, pp. 1879–1890, Sep. 2023, doi: 10.1007/S12524-022-01495-X.

[23] A. Shah *et al.*, "Comparative analysis of median filter and its variants for removal of impulse noise from gray scale images," *J. King Saud Univ. - Comput. Inf. Sci.*, vol. 34, no. 3, pp. 505–519, Mar. 2022, doi: 10.1016/j.jksuci.2020.03.007.

[24] S. Khare and P. Kaushik, "Speckle filtering of ultrasonic images using weighted nuclear norm minimization in wavelet domain," *Biomed. Signal Process. Control*, vol. 70, no. November 2020, p. 102997, Sep. 2021, doi: 10.1016/j.bspc.2021.102997.

[25] M. R. Prerna Singh and R. De Ryke, "Feature Enhancement in Medical Ultrasound Videos Using Multifractal and Contrast Adaptive Histogram Equalization Techniques," *Proc. - 2nd Int. Conf. Multimed. Inf. Process. Retrieval, MIPR 2019*, pp. 240–245, 2019, doi: 10.1109/MIPR.2019.00050.

[26] A. M. Reza, "Realization of the contrast limited adaptive histogram equalization (CLAHE) for real-time image enhancement," *J. VLSI Signal Process. Syst. Signal Image. Video Technol.*, vol. 38, no. 1, pp. 35–44, 2004, doi: 10.1023/B:VLSI.0000028532.53893.82.

[27] Priyanka and D. Kumar, "Feature Extraction and Selection of kidney Ultrasound Images Using GLCM and PCA," *Procedia Comput. Sci.*, vol. 167, no. 2019, pp. 1722–1731, 2020, doi: 10.1016/j.procs.2020.03.382.

[28] R. Ahmad and B. K. Mohanty, "Chronic kidney disease stage identification using texture analysis of ultrasound images," *Biomed. Signal Process. Control*, vol. 69, no. June, p. 102695, 2021, doi: 10.1016/j.bspc.2021.102695.

[29] S. Vani Kumari and K. Usha Rani, "Analysis on Various Feature Extraction Methods for Medical Image Classification," in *Learning and Analytics in Intelligent Systems*, 2020, no. 16, pp. 19–31, doi: 10.1007/978-3-030-46943-6_3.

[30] S. Pavithra, R. Vanithamani, and J. Justin, "Computer aided breast cancer detection using ultrasound images," *Mater. Today Proc.*, vol. 33, pp. 4802–4807, 2020, doi: 10.1016/j.matpr.2020.08.381.

[31] R. M. Haralick, I. Dinstein, and K. Shanmugam, "Textural Features for Image Classification," *IEEE Trans. Syst. Man Cybern.*, vol. SMC-3, no. 6, pp. 610–621, 1973, doi: 10.1109/TSMC.1973.4309314.

[32] S. Bahri, Suprijanto, and E. Juliastuti, "Texture Analysis of Ultrasound Images to Differentiate Pneumonia and Covid-19," *2021 IEEE Int. Biomed. Instrum. Technol. Conf. Improv. Healthc. Technol. to Achieve Univers. Heal. Cover. IBITeC 2021*, pp. 24–28, 2021, doi: 10.1109/IBITeC53045.2021.9649067.

[33] Y. Wang, Y. Zhang, Q. He, H. Liao, and J. Luo, "Quantitative Analysis of Pleural Line and B-Lines in Lung Ultrasound Images for Severity Assessment of COVID-19 Pneumonia," *IEEE Trans. Ultrason. Ferroelectr. Freq. Control*, vol. 69, no. 1, pp. 73–83, 2022, doi: 10.1109/TUFFC.2021.3107598.

[34] M. Galar, A. Fernández, E. Barrenechea, H. Bustince, and F. Herrera, "An overview of ensemble methods for binary classifiers in multi-class problems: Experimental study on one-vs-one and one-vs-all schemes," *Pattern Recognit.*, vol. 44, no. 8, pp. 1761–1776, 2011, doi: 10.1016/j.patcog.2011.01.017.

[35] M. Bansal, M. Kumar, and M. Kumar, "2D object recognition: a comparative analysis of SIFT, SURF and ORB feature descriptors," *Multimed. Tools Appl.*, vol. 80, no. 12, pp. 18839–18857, 2021, doi: 10.1007/s11042-021-10646-0.

[36] R. Kaur, M. Juneja, and A. K. Mandal, "Machine learning based quantitative texture analysis of CT images for diagnosis of renal lesions," *Biomed. Signal Process. Control*, vol. 64, 2021, doi: 10.1016/j.bspc.2020.102311.

[37] H. Zhang, "The optimality of Naive Bayes," *Proc. Seventeenth Int. Florida Artif. Intell. Res. Soc. Conf. FLAIRS 2004*, vol. 2, pp. 1-6, 2004. [Online]. Available at: https://aaai.org/papers/flairs-2004-097/.

[38] G. Muhammad and M. Shamim Hossain, "COVID-19 and Non-COVID-19 Classification using Multi-layers Fusion From Lung Ultrasound Images," *Inf. Fusion*, vol. 72, no. November 2020, pp. 80–88, 2021, doi: 10.1016/j.inffus.2021.02.013.

[39] B. Barros and P. Lacerda, "Pulmonary COVID-19 : Learning Spatiotemporal Features Combining CNN and LSTM Networks for Lung Ultrasound Video Classification," *Sensors*, vol. 21, no. 5486, pp. 1–25, 2021, doi: 10.3390/s21165486.

[40] F. Sadik, A. G. Dastider, and S. A. Fattah, "SpecMEn-DL: spectral mask enhancement with deep learning models to predict COVID-19 from lung ultrasound videos," *Heal. Inf. Sci. Syst.*, vol. 9, no. 1, pp. 1–11, 2021, doi: 10.1007/s13755-021-00154-8.

[41] N. Awasthi, A. Dayal, L. R. Cenkeramaddi, and P. K. Yalavarthy, "Mini-COVIDNet: Efficient Lightweight Deep Neural Network for Ultrasound Based Point-of-Care Detection of COVID-19," *IEEE Trans. Ultrason. Ferroelectr. Freq. Control*, vol. 68, no. 6, pp. 2023–2037, 2021, doi: 10.1109/TUFFC.2021.3068190.

[42] J. Born *et al.*, "Accelerating detection of lung pathologies with explainable ultrasound image analysis," *Appl. Sci.*, vol. 11, no. 2, pp. 1–23, 2021, doi: 10.3390/app11020672.